Article

Quantum error correction of qudits beyond break-even

https://doi.org/10.1038/s41586-025-08899-y

Received: 2 October 2024

Accepted: 14 March 2025

Published online: 14 May 2025

Open access

Check for updates

Benjamin L. Brock[1,2,3]✉, Shraddha Singh[1,2,3], Alec Eickbusch[1,2,3,4], Volodymyr V. Sivak[1,2,3,4], Andy Z. Ding[1,2,3], Luigi Frunzio[1,2,3], Steven M. Girvin[1,2,3] & Michel H. Devoret[1,2,3,5]✉

Hilbert space dimension is a key resource for quantum information processing[1,2]. Not only is a large overall Hilbert space an essential requirement for quantum error correction, but a large local Hilbert space can also be advantageous for realizing gates and algorithms more efficiently[3–7]. As a result, there has been considerable experimental effort in recent years to develop quantum computing platforms using qudits (d-dimensional quantum systems with $d > 2$) as the fundamental unit of quantum information[8–19]. Just as with qubits, quantum error correction of these qudits will be necessary in the long run, but so far, error correction of logical qudits has not been demonstrated experimentally. Here we report the experimental realization of an error-corrected logical qutrit ($d = 3$) and ququart ($d = 4$), which was achieved with the Gottesman–Kitaev–Preskill bosonic code[20]. Using a reinforcement learning agent[21,22], we optimized the Gottesman–Kitaev–Preskill qutrit (ququart) as a ternary (quaternary) quantum memory and achieved beyond break-even error correction with a gain of 1.82 ± 0.03 (1.87 ± 0.03). This work represents a novel way of leveraging the large Hilbert space of a harmonic oscillator to realize hardware-efficient quantum error correction.

The number of quantum states available to a quantum computer, quantified by its Hilbert space dimension, is a fundamental and precious resource[1,2]. Crucially, the goal of achieving quantum advantage at scale relies on the ability to manipulate an exponentially large Hilbert space with subexponentially many operations. This large Hilbert space is typically realized using N qubits (two-level quantum systems), giving rise to a 2^N-dimensional Hilbert space. However, most physical realizations of qubits have many more than two available states. These valuable extra quantum states often go untapped, because the methods for working with qudits (d-level quantum systems with $d > 2$) as the fundamental unit of quantum information are more complicated and less well developed than those for working with qubits[23].

On the other hand, embracing these qudits could enable more efficient distillation of magic states[24,25], synthesis of gates[3,4], compilation of algorithms[5–7], and simulation of high-dimensional quantum systems[26,27]. For these reasons, considerable experimental effort has been spent in recent years on developing qudit-based platforms for quantum computing, using donor spins in silicon[8], ultracold atoms and molecules[9,10], optical photons[11,12], superconducting circuits[13–15], trapped ions[16,17], and vacancy centers[18,19]. If qudits are to be useful in the long run, however, quantum error correction (QEC) will be necessary.

In this work we experimentally demonstrate QEC of logical qudits with $d > 2$, using the Gottesman–Kitaev–Preskill (GKP) bosonic code[20] to realize a logical qutrit ($d = 3$) and ququart ($d = 4$) encoded in grid states of an oscillator. Our optimized GKP qutrit (ququart) lived longer, on average, than the best physical qutrit (ququart) available in our system by a factor of 1.82 ± 0.03 (1.87 ± 0.03), making this one of only a handful of experiments to beat the break-even point of QEC for quantum memories[22,28–30]. This experiment represents a novel way of leveraging the large Hilbert space of an oscillator and builds on previous realizations of GKP qubits[22,31–36] and bosonic codes[28,29,37]. Access to a higher-dimensional error-corrected manifold of quantum states may enable more hardware-efficient architectures for quantum information processing.

Error correction of GKP qudits

Our experimental device is the same as in ref. 22 and consists of a tantalum transmon[38,39] dispersively coupled to a three-dimensional superconducting microwave cavity[40], as shown in Fig. 1a. The cavity hosts an oscillator mode (described by Fock states $\{|n\rangle : n \in \mathbb{Z}_{\geq 0}\}$ and mode operator a), which is used for storing our logical GKP states. The transmon hosts a qubit (described by ground and excited states $\{|g\rangle, |e\rangle\}$ and Pauli operators $\sigma_{x,y,z}$), which is used as an ancilla for controlling the oscillator and performing error correction. The cavity has an energy relaxation lifetime of $T_{1,\mathrm{c}} = 631$ μs and Ramsey coherence time $T_{2\mathrm{R,c}} = 1{,}030$ μs, whereas the transmon has lifetime $T_{1,\mathrm{q}} = 295$ μs and Hahn-echo lifetime $T_{2\mathrm{E,q}} = 286$ μs (Supplementary Information section I).

We employed the single-mode square GKP code[20], which is designed to be translationally symmetric in phase space. The structure of the

[1]Department of Applied Physics, Yale University, New Haven, CT, USA. [2]Yale Quantum Institute, Yale University, New Haven, CT, USA. [3]Department of Physics, Yale University, New Haven, CT, USA. [4]Present address: Google Quantum AI, Santa Barbara, CA, USA. [5]Present address: UC Santa Barbara Department of Physics and Google Quantum AI, Santa Barbara, CA, USA. ✉e-mail: benjamin.brock@yale.edu; michel.devoret@yale.edu

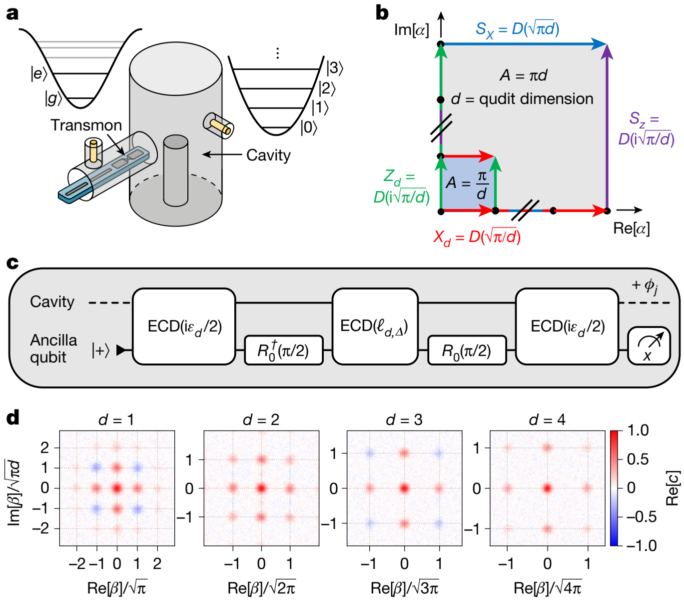

Fig. 1 | Stabilizing GKP qudits. a, Schematic of the experimental device. **b**, Geometric structure of the displacement operators that define the single-mode square GKP code. **c**, Circuit for one round of finite-energy GKP qudit stabilization, generalizing the SBS protocol[43]. The big ECD gate[48] of amplitude $\ell_{d,\Delta} = \sqrt{\pi d}\cosh(\Delta^2)$ is approximately the stabilizer length. The small ECD gates of amplitude $\varepsilon_d/2 = \sqrt{\pi d}\sinh(\Delta^2)/2$ account for the envelope size Δ. At the end of SBS round j, the cavity phase is updated by ϕ_j (Methods). **d**, Measured real part of the characteristic function of the maximally mixed GKP qudit state for $d = 1$ to 4 with $\Delta = 0.3$, prepared by performing 300 SBS rounds starting from the cavity in its vacuum state $|0\rangle$.

code comes from the geometric phase associated with displacement operators $D(\alpha) = \exp(\alpha a^\dagger - \alpha^* a)$ in phase space, as depicted in Fig. 1b. Two displacements commute up to a phase given by twice the area A they enclose, such that $D(\alpha_1)D(\alpha_2) = \exp(2iA)D(\alpha_2)D(\alpha_1)$ with $A = \mathrm{Im}[\alpha_1\alpha_2^*]$. The ideal code has stabilizer generators $S_X = D(\ell_d)$ and $S_Z = D(i\ell_d)$, where ℓ_d is the stabilizer length. If these stabilizers are to have a common +1 eigenspace (the code space), they must commute, which means they must enclose an area πd in phase space for positive integer d, such that $\ell_d = \sqrt{\pi d}$, where d is the dimension of the code space. The code words of this idealized logical qudit are grids of position eigenstates $|q\rangle$, with form

$$|Z_n\rangle_d \propto \sum_{k=-\infty}^{\infty} |q = n\sqrt{2\pi/d} + k\sqrt{2\pi d}\rangle, \tag{1}$$

where $n = 0, 1, ..., d-1$ and $q = (a + a^\dagger)/\sqrt{2}$ is the position operator. Note that with our choice of phase-space units, translations in position and displacements along the real axis of phase space differ in amplitude by a factor of $\sqrt{2}$. The logical operators of the ideal code are the displacement operators $X_d = D(\sqrt{\pi/d})$ and $Z_d = D(i\sqrt{\pi/d})$, which act on the code space as

$$\begin{aligned} Z_d\,|Z_n\rangle_d &= (\omega_d)^n |Z_n\rangle_d, \\ X_d\,|Z_n\rangle_d &= |Z_{(n+1)\bmod d}\rangle_d, \end{aligned} \tag{2}$$

where $\omega_d = \exp(2\pi i/d)$ is the primitive dth root of unity. These operators Z_d and X_d are the generalized Pauli operators[41,42], which are unitary but no longer Hermitian for $d > 2$. These operators obey the generalized commutation relation $Z_dX_d = \omega_d X_d Z_d$, determined by the area these displacements enclose in phase space. Compared to GKP qubits, GKP qudits have a longer stabilizer length that is proportional to $\sqrt{d}$, such that they encode information further out in phase space, and a shorter distance between logical states that is proportional to $1/\sqrt{d}$.

In practice, we work with an approximate finite-energy version of this code, which is obtained by applying the Gaussian envelope operator $E_\Delta = \exp(-\Delta^2 a^\dagger a)$ to both the operators and states of the ideal code[43,44]. The parameter Δ determines both the squeezing of individual quadrature peaks in the grid states as well as their overall extent in energy. For smaller Δ, the peaks are more highly squeezed and the states have more energy. On increasing d, we expect to require smaller Δ, as the logical states are more closely spaced and contain information further out in phase space (at higher energies). With smaller Δ, we expect the lifetime of our GKP qudits to decrease, as having more energy amplifies the rate of oscillator photon loss, and having information stored further out in phase space amplifies the effects of oscillator dephasing.

To stabilize the finite-energy GKP qudit manifold, we adapted the small-big-small (SBS) protocol[43] to the stabilizer length $\ell_d = \sqrt{\pi d}$, as shown in Fig. 1c. This circuit, consisting of echoed conditional displacement (ECD) gates $\mathrm{ECD}(\beta) = D(\beta/2)|e\rangle\langle g| + D(-\beta/2)|g\rangle\langle e|$ and ancilla qubit rotations $R_\varphi(\theta) = \exp[i(\sigma_x \cos\varphi + \sigma_y \sin\varphi)\theta/2]$, realizes an engineered dissipation onto the finite-energy GKP qudit manifold that removes the entropy associated with physical errors in the oscillator before they can accumulate into logical errors (Supplementary Information section II-A)[32,43]. In these expressions, β is the complex amplitude of the conditional displacement, φ is the azimuthal angle defining the rotation axis and θ is the rotation angle. This protocol is autonomous, requiring only a reset of the ancilla between rounds. We update the reference phase of the cavity mode between rounds to stabilize both quadratures in phase space (Methods).

To verify that this generalized SBS protocol works, we ran it for 300 rounds, starting with the cavity in vacuum, which prepared the maximally mixed state of the finite-energy GKP qudit $\rho_d^{\mathrm{mix}} = (1/d)\sum_{n=0}^{d-1}|Z_n\rangle\langle Z_n|_d$. We performed characteristic function tomography[45] of ρ_d^{mix} prepared in this way, the results of which are shown in Fig. 1d. As expected from its definition $\mathcal{C}(\beta) = \langle D(\beta)\rangle$, the characteristic function of these states has peaks at the stabilizer lengths, which increase with d according to $\ell_d = \sqrt{\pi d}$. The negative regions of $\mathrm{Re}[\mathcal{C}(\beta)]$ for odd d are a consequence of the geometric phase associated with displacement operators $D(e^{i\pi/4}\sqrt{2\pi d}) = (-1)^d D(\sqrt{\pi d})D(i\sqrt{\pi d})$. However, it is interesting to note that the states ρ_d^{mix} for odd d have regions of Wigner negativity (Supplementary Information section II-B) and are, therefore, non-classical[46].

Characterizing quantum memories

To characterize the performance of our logical qudits as quantum memories and establish the concept of QEC gain for qudits, we followed previous work[22] and used the average channel fidelity $\mathcal{F}_d(\mathcal{E}, I)$, which quantifies how well a channel $\mathcal{E}$ realizes the identity I (ref. 47). Although $\mathcal{F}_d$ will have a non-exponential time evolution in general, it can always be expanded to short times dt as $\mathcal{F}_d(\mathcal{E}, I) \approx 1 - ((d-1)/d)\Gamma dt$, where Γ is the effective decay rate of the channel $\mathcal{E}$ at short times. This rate Γ enables us to compare different decay channels on the same footing. In particular, we want to compare the decay rate $\Gamma_d^{\mathrm{logical}}$ of our logical qudit to $\Gamma_d^{\mathrm{physical}}$ of the best physical qudit in our system. We define the QEC gain as their ratio $G_d = \Gamma_d^{\mathrm{physical}}/\Gamma_d^{\mathrm{logical}}$, and the break-even point is when this gain is unity.

The average channel fidelity can be expressed in terms of the probabilities $\langle\psi|\mathcal{E}(|\psi\rangle\langle\psi|)|\psi\rangle_d$ that our error-correction channel $\mathcal{E}$ preserves the qudit state $|\psi\rangle_d$, summed over a representative set of states $\{|\psi\rangle_d\}$ (Supplementary Information section III). Each of these probabilities entails a separate experiment in which we prepare the state $|\psi\rangle_d$, perform error correction, and measure our logical qudit in a basis containing $|\psi\rangle_d$. Herein lies the primary experimental challenge of the present

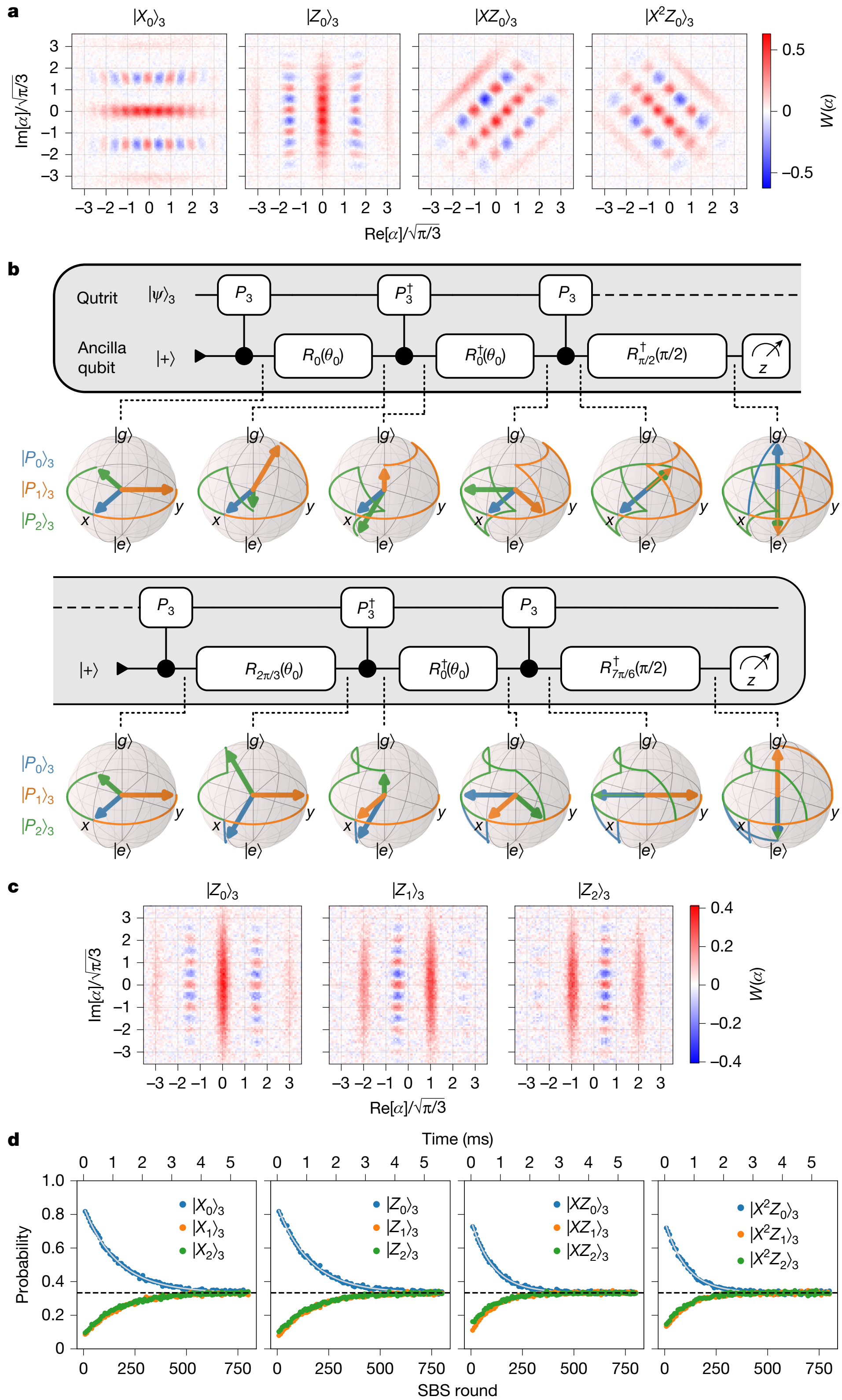

Fig. 2 | Realization of a logical GKP qutrit. a, State preparation of qutrit Pauli eigenstates $|P_0\rangle_3$ with $\Delta = 0.32$. **b**, Circuit for measuring a qutrit in the basis of Pauli operator P_3 using an ancilla qubit, where $\theta_0 = 2\arctan(1/\sqrt{2})$. The first measurement distinguishes between the state $|P_0\rangle_3$ and the subspace $\{|P_1\rangle_3, |P_2\rangle_3\}$, whereas the second distinguishes between $|P_1\rangle_3$ and $\{|P_0\rangle_3, |P_2\rangle_3\}$. The Bloch spheres depict the trajectories taken by the ancilla when the qutrit is in each Pauli eigenstate. **c**, Backaction of the qutrit Pauli measurement in the Z_3 basis, applied to the maximally mixed qutrit state. **d**, Decay of qutrit Pauli eigenstates $|P_0\rangle_3$ under the optimized QEC protocol. The dashed black lines indicate a probability of 1/3. The solid grey lines are exponential fits. From left to right, we found $\gamma_{X_0}^{-1} = 1{,}153 \pm 13$ μs, $\gamma_{Z_0}^{-1} = 1{,}120 \pm 15$ μs, $\gamma_{XZ_0}^{-1} = 743 \pm 10$ μs and $\gamma_{X^2Z_0}^{-1} = 727 \pm 11$ μs.

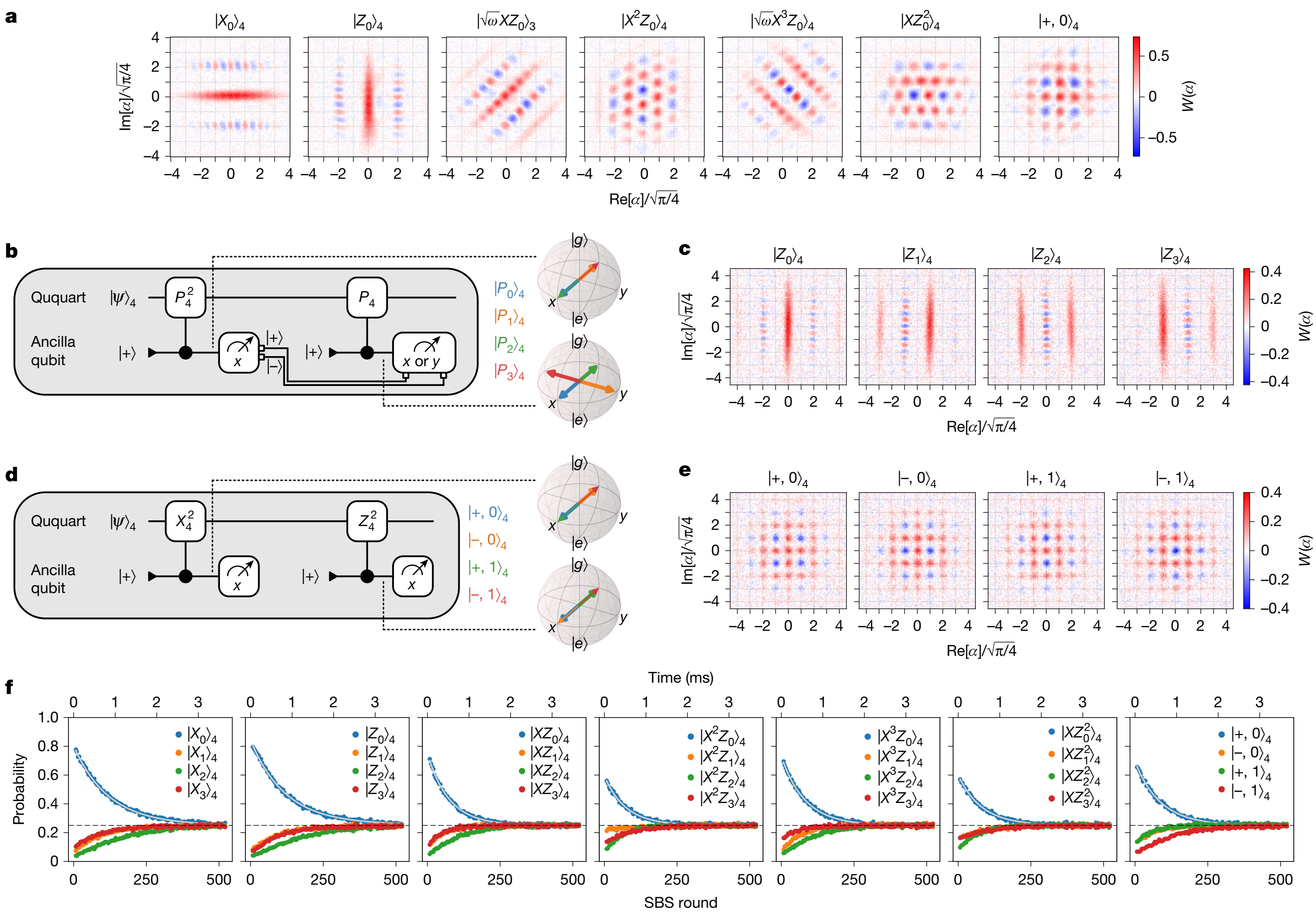

Fig. 3 | Realization of a logical GKP ququart. a, State preparation of ququart Pauli eigenstates $|P_0\rangle_4$ and parity state $|+,0\rangle_4$ with $\Delta = 0.32$. **b**, Circuit for measuring a ququart in the basis of Pauli operator P_4 using an ancilla qubit. The first measurement distinguishes between the even and odd states $|P_{\text{even/odd}}\rangle_4$, and the second measurement distinguishes between the remaining two states. The Bloch spheres depict the trajectories taken by the ancilla when the ququart is in each Pauli eigenstate. **c**, Backaction of the GKP ququart Pauli measurement in the Z_4 basis applied to the maximally mixed ququart state. **d**, Circuit for measuring a ququart in the parity basis $\{|\pm, m\rangle_4 : m = 0, 1\}$, where $X_4^2|\pm, m\rangle_4 = \pm|\pm, m\rangle_4$ and $Z_4^2\,|\pm, m\rangle_4 = (-1)^m|\pm, m\rangle_4$. The first measurement determines the eigenvalue of X_4^2, and the second determines that of Z_4^2. **e**, Backaction of the GKP ququart parity measurement applied to the maximally mixed ququart state. **f**, Decay of ququart Pauli eigenstates $|P_0\rangle_4$ and parity state $|+,0\rangle_4$ under the optimized QEC protocol. The dashed black lines indicate a probability of 1/4. The solid grey lines are exponential fits. From left to right, we found $\gamma_{X_0}^{-1} = 840 \pm 8$ μs, $\gamma_{Z_0}^{-1} = 836 \pm 9$ μs, $\gamma_{XZ_0}^{-1} = 519 \pm 6$ μs, $\gamma_{X^2Z_0}^{-1} = 507 \pm 9$ μs, $\gamma_{X^3Z_0}^{-1} = 571 \pm 7$ μs, $\gamma_{XZ_0^2}^{-1} = 562 \pm 9$ μs and $\gamma_{+,0}^{-1} = 607 \pm 8$ μs.

work: devising ways of measuring our logical GKP qudit in bases containing each state in our representative set $\{|\psi\rangle_d\}$ using only binary measurements of our ancilla qubit.

For the qutrit in $d = 3$, our representative set of states are the bases $\{|P_n\rangle_3 : n = 0, 1, 2\}$ of Pauli operators $P \in \mathcal{P}_3 = \{X_3, Z_3, X_3Z_3, X_3^2Z_3\}$, defined by $P|P_n\rangle_3 = \omega^n|P_n\rangle_3$ for $\omega = \exp(2\pi i/3)$. The effective decay rate of our logical GKP qutrit can then be expressed as

$$\Gamma_3^{\text{GKP}} = \frac{1}{12}\sum_{P\in\mathcal{P}_3}\sum_{n=0}^{2}\gamma_{P_n}, \tag{3}$$

where γ_{P_n} is the rate at which the state $|P_n\rangle_3$ decays to ρ_3^{mix}. For the ququart in $d = 4$, our representative set of states consists of two types of bases. The first type are the bases $\{|P_n\rangle_4 : n = 0, 1, 2, 3\}$ of Pauli operators $P \in \mathcal{P}_4 = \{X_4, Z_4, \sqrt{\omega}X_4Z_4, X_4^2Z_4, \sqrt{\omega}X_4^3Z_4, X_4Z_4^2\}$, defined by $P|P_n\rangle_4 = \omega^n|P_n\rangle_4$ for $\omega = i$. The second type is what we call the ququart parity basis $\{|\pm, m\rangle_4 : m = 0, 1\}$ consisting of the simultaneous eigenstates of X_4^2 and Z_4^2, such that $X_4^2|\pm, m\rangle_4 = \pm|\pm, m\rangle_4$ and $Z_4^2|\pm, m\rangle_4 = (-1)^m|\pm, m\rangle_4$. The effective decay rate of our logical GKP ququart can then be expressed as

$$\Gamma_4^{\text{GKP}} = \frac{1}{20}\left[\sum_{P\in\mathcal{P}_4}\sum_{n=0}^{3}\gamma_{P_n} - \sum_{\substack{s=\pm\\ m=0,1}}\gamma_{\pm,m}\right], \tag{4}$$

where γ_{P_n} ($\gamma_{\pm,m}$) is the rate at which the Pauli eigenstate $|P_n\rangle_4$ (parity state $|\pm, m\rangle_4$) decays to ρ_4^{mix}.

As a basis of comparison, the best physical qudit in our system is the cavity Fock qudit spanned by the states $|0\rangle, |1\rangle, ..., |d-1\rangle$. The cavity hosting this qudit decoheres under both photon loss and pure dephasing at rates $\kappa_{1,\text{c}} = 1/T_{1,\text{c}}$ and $\kappa_{\phi,\text{c}} = 1/T_{2\text{R},\text{c}} - 1/2T_{1,\text{c}}$. From these measured rates, we can extrapolate the effective decay rate Γ_d^{Fock} of the cavity Fock qudit under these decoherence channels. For $d = 2$ through 4, we obtained $\Gamma_2^{\text{Fock}} = (851 \pm 9\ \mu\text{s})^{-1}$, $\Gamma_3^{\text{Fock}} = (488 \pm 7\ \mu\text{s})^{-1}$ and $\Gamma_4^{\text{Fock}} = (332 \pm 6\ \mu\text{s})^{-1}$.

Logical qutrit beyond break-even

To measure the effective decay rate of the logical GKP qutrit through equation (3), we needed to prepare all of the eigenstates of the

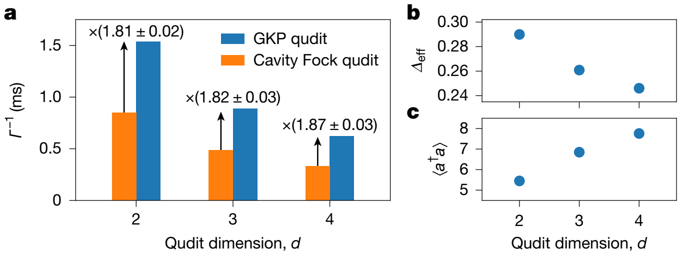

Fig. 4 | Comparing GKP qudits. **a**, Effective lifetime of the physical cavity Fock qudit and logical GKP qudit for $d \in \{2, 3, 4\}$. The arrows indicate the QEC gain. **b**, Effective envelope size Δ_{eff} of the optimized GKP qudit for $d \in \{2, 3, 4\}$. **c**, Mean number of photons in the cavity for the optimized GKP qudit for $d \in \{2, 3, 4\}$.

Pauli operators in $\mathcal{P}_3$ and perform measurements in the basis of these Pauli operators. To prepare the eigenstates $|P_n\rangle_3$, we used interleaved sequences of ECD gates and transmon rotations, which enable universal control of the oscillator mode in the cavity[48]. We optimized depth-8 ECD circuits to implement the unitary that maps the cavity vacuum state $|0\rangle$ to the desired state $|P_n\rangle_3$ with envelope size $\Delta = 0.32$. The measured Wigner functions $W(\alpha) = \langle D(\alpha)e^{i\pi a^\dagger a}D(-\alpha)\rangle$ of our prepared $|P_0\rangle_3$ states are shown in Fig. 2a (see Supplementary Information section V-A for the other eigenstates). In general, the eigenstates $|P_n\rangle_d$ are oriented in phase space in the direction of the displacement induced by P_d, where X_d displaces rightward, Z_d displaces upward, and $P_d^{d-1} = P_d^{-1}$.

We measured the GKP qutrit in Pauli basis P_3 using the circuit shown in Fig. 2b. The generalized ancilla-qubit-controlled Pauli operators $CP_3 = |g\rangle\langle g|I_3 + |e\rangle\langle e|P_3$ were realized with ECD gates, where I_d is the identity operator in dimension d. Intuitively, as generalized Pauli operators on GKP qudits are implemented through displacements, the conditional versions of these displacements implement CP_d operations, with some technical caveats (Methods). The idea of this circuit is to perform a projective measurement in the P_3 basis using two binary measurements of the ancilla qubit. The first measurement determines whether the qutrit is in state $|P_0\rangle_3$ or the $\{|P_1\rangle_3, |P_2\rangle_3\}$ subspace, and the second determines whether the qutrit is in state $|P_1\rangle_3$ or the $\{|P_0\rangle_3, |P_2\rangle_3\}$ subspace. These two binary measurements uniquely determine the ternary measurement result in the P_3 basis and collapse the qutrit state accordingly. Note that this circuit was constructed for the ideal code and incurs infidelity when applied to the finite-energy code. To verify that this circuit realizes the desired projective measurement, we prepared ρ_3^{mix}, measured in the Z_3 basis, and performed Wigner tomography of the cavity post-selected on the three measurement outcomes. The results of this measurement are shown in Fig. 2c (see Supplementary Information section V-B for the other Pauli bases).

With these techniques, we used a reinforcement learning agent[21] to optimize the logical GKP qutrit as a ternary quantum memory following the method in ref. 22 (Methods). We then evaluated the optimal QEC protocol by preparing each eigenstate $|P_n\rangle_3$ for each $P_3 \in \mathcal{P}_3$, implementing the optimized QEC protocol for a variable number of rounds, and measuring the final state in the P_3 basis. Finally, we fitted an exponential decay to each probability $\langle P_n|\mathcal{E}(|P_n\rangle\langle P_n|)|P_n\rangle$ to obtain γ_{P_n}. The results of this evaluation for the $|P_0\rangle_3$ states are shown in Fig. 2d (the other results are given in Supplementary Information section V-C). As with the GKP qubit[22,33], we found longer lifetimes for the 'Cartesian' eigenstates of X_3 and Z_3 than for the remaining 'diagonal' eigenstates, as the latter were more susceptible to both cavity photon-loss errors and ancilla bit-flip errors[33]. Using equation (3) with our measured rates γ_{P_n}, we obtained $\Gamma_3^{\mathrm{GKP}} = (886 \pm 3\ \mu\mathrm{s})^{-1}$. Comparing with Γ_3^{Fock}, we obtained the QEC gain

$$G_3 = \Gamma_3^{\mathrm{Fock}}/\Gamma_3^{\mathrm{GKP}} = 1.82 \pm 0.03, \tag{5}$$

which is well beyond the break-even point.

Logical ququart beyond break-even

We followed a similar procedure to measure the effective decay rate of our logical GKP ququart through equation (4) as we did for the qutrit, the main difference being that we needed to prepare and measure states in both the ququart parity basis and the Pauli bases $P \in \mathcal{P}_4$. We again used depth-8 ECD circuits[48] to prepare the Pauli eigenstates $|P_n\rangle_4$ and parity states $|\pm, m\rangle_4$ with $\Delta = 0.32$. The measured Wigner functions of our prepared $|P_0\rangle_4$ states and the $|+, 0\rangle_4$ state are shown in Fig. 3a (see Supplementary Information section VI-A for the remaining states). Again, the eigenstates $|P_n\rangle_d$ are oriented in phase space in the direction of the displacement induced by P_d. By contrast, the parity states $|\pm, m\rangle$ are uniform grids, equally oriented both horizontally and vertically.

We measured the GKP ququart in Pauli basis P_4 using the circuit shown in Fig. 3b. The first binary measurement of the ancilla qubit distinguishes between the even subspace $\{|P_0\rangle, |P_2\rangle\}$ and odd subspace $\{|P_1\rangle, |P_3\rangle\}$ by measuring whether $P_4^2 = \pm 1$, and the second distinguishes between the remaining two states by measuring $P_4 = \pm 1$ (if in the even subspace) or $P_4 = \pm \mathrm{i}$ (if in the odd subspace). To verify that this circuit realizes the desired projective measurement, we prepared ρ_4^{mix}, measured in the Z_4 basis, and performed Wigner tomography of the cavity post-selected on the four measurement outcomes. The results of this measurement are shown in Fig. 3c (see Supplementary Information section VI-B for the other Pauli bases).

We measured the GKP ququart in the parity basis $\{|\pm, m\rangle_4 : m = 0, 1\}$ using the circuit shown in Fig. 3d. The first binary measurement of the ancilla qubit determines whether $X_4^2 = \pm 1$, and the second determines whether $Z_4^2 = \pm 1$. To verify this circuit realizes the desired projective measurement, we prepared ρ_4^{mix}, measured in the parity basis, and performed Wigner tomography post-selected on the four measurement outcomes. The results of this measurement are shown in Fig. 3e. As with the qutrit, our logical ququart measurements were constructed for the ideal code, and they incur infidelity when applied to the finite-energy code.

With these techniques, we again used a reinforcement learning agent[21] to optimize the logical GKP ququart as a quaternary quantum memory following the method in ref. 22 (Methods). We then evaluated the optimal QEC protocol by preparing each eigenstate $|P_n\rangle_4$ for each $P_4 \in \mathcal{P}_4$ (plus the parity basis), implementing the optimized QEC protocol for a variable number of rounds, and measuring the final state in its corresponding basis. Finally, we fitted an exponential decay to each probability $\langle P_n|\mathcal{E}(|P_n\rangle\langle P_n|)|P_n\rangle$ and $\langle \pm, m|\ \mathcal{E}(|\pm, m\rangle\langle \pm, m|)|\pm, m\rangle$ to obtain γ_{P_n} and $\gamma_{\pm,m}$, respectively. The results of this evaluation for the $|P_0\rangle_4$ states and $|+, 0\rangle_4$ state are shown in Fig. 3f (the remaining results are given in Supplementary Information section VI-C). Again, we found longer lifetimes for the Cartesian eigenstates of X_4 and Z_4 than for the remaining eigenstates. Using equation (4) with our measured rates γ_{P_n} and $\gamma_{\pm,m}$, we obtained $\Gamma_4^{\mathrm{GKP}} = (620 \pm 2\ \mu\mathrm{s})^{-1}$. Comparing with Γ_4^{Fock}, we obtained the QEC gain

$$G_4 = \Gamma_4^{\mathrm{Fock}}/\Gamma_4^{\mathrm{GKP}} = 1.87 \pm 0.03, \tag{6}$$

which is, again, well beyond the break-even point.

Discussion

Notably, despite the increasing complexity of the code, we found that the QEC gain stayed roughly constant at about 1.8 as we increased the dimension of our logical GKP qudit from 2 to 4, as shown in Fig. 4a. Note that the gain $G_2 = 1.81 \pm 0.02$ that we achieved with the GKP qubit is less than the gain of 2.3 previously reported using the same device[22], which was due to changes in both the device and the experimental conditions (see Supplementary Information section IV-C for details). Regardless, the measurements shown in Fig. 4a were taken under the same conditions, and they indicate that as we increased d from 2 to 4, the lifetime of our logical GKP qudit decreased at about the same rate as that of our cavity Fock qudit.

This decrease occurred because the GKP qudit states are more closely spaced and contain information further out in phase space for increasing d, which should require smaller Δ. To verify this, we prepared ρ_d^{mix} of our optimal GKP qudits and measured the central Gaussian peak of their characteristic functions for $d = 2$ through 4 (Supplementary Information). The width Δ_{eff} of this Gaussian is related to the parameter Δ and decreased with d, as shown in Fig. 4b, in agreement with our expectations. The average number of photons $\langle a^\dagger a\rangle$ in ρ_d^{mix} can also be inferred from this measurement of Δ_{eff} and is presented in Fig. 4c.

With a smaller Δ, our logical GKP qudits had more energy and were more highly squeezed, which should amplify the rates of cavity photon loss and dephasing. To corroborate this, we simulated our optimal QEC protocols and isolated the relative contributions of different physical errors to our overall logical error rates (Supplementary Information section VII). We found that the three largest sources of logical errors were transmon bit flips, whose relative contribution decreased as d was increased, cavity photon loss, whose relative contribution increased as d was increased, and cavity dephasing, which was the dominant source of error and whose relative contribution increased as d was increased. As our cavity dephasing was primarily due to the thermal population $n_{\mathrm{th}} = 2.2 \pm 0.1\%$ of the transmon[40], the lifetimes of our logical GKP qudits could be substantially improved by either reducing n_{th} or using an ancilla that can be actively decoupled from the cavity when not in use[49,50].

In summary, we have demonstrated QEC of logical qudits with $d > 2$, which represents a milestone achievement in the development of qudits for useful quantum technologies. Moreover, we have beaten the break-even point for QEC of quantum memories, a result few other experiments have accomplished[22,28–30]. These results rely upon many technical advances, such as our generalization of previous experimental methods[22] and our invention of protocols for measuring qudits in generalized Pauli bases. Our work builds on the promise of hardware efficiency offered by bosonic codes[22,28,29,31–37] and represents a novel way of leveraging the large Hilbert space of an oscillator. In exchange for a modest reduction in lifetime, we gained access to more logical quantum states in a single physical system. This could enable more efficient compilation of gates[3,4] and algorithms[5–7], alternative techniques for quantum communication[51] and transduction[52], and advantageous strategies for concatenation into an external multi-qudit code[24,25]. Such a concatenation requires entangling gates, which for GKP qudits can be realized with the same operations used for entangling GKP qubits[20,53–55]. With the realization of bosonic logical qudits, we have also established a platform for concatenating codes internally. By embedding a logical qubit within a bosonic logical qudit[20,56–58], multiple layers of error correction can be implemented inside a single oscillator.

Online content

Any methods, additional references, Nature Portfolio reporting summaries, source data, extended data, supplementary information, acknowledgements, peer review information; details of author contributions and competing interests; and statements of data and code availability are available at https://doi.org/10.1038/s41586-025-08899-y.

1. Blume-Kohout, R., Caves, C. M. & Deutsch, I. H. Climbing mount scalable: physical resource requirements for a scalable quantum computer. *Found. Phys.* **32**, 1641–1670 (2002).
2. Greentree, A. D. et al. Maximizing the Hilbert space for a finite number of distinguishable quantum states. *Phys. Rev. Lett.* **92**, 097901 (2004).
3. Ralph, T. C., Resch, K. J. & Gilchrist, A. Efficient Toffoli gates using qudits. *Phys. Rev. A* **75**, 022313 (2007).
4. Fedorov, A., Steffen, L., Baur, M., Da Silva, M. P. & Wallraff, A. Implementation of a Toffoli gate with superconducting circuits. *Nature* **481**, 170–172 (2012).
5. Bocharov, A., Roetteler, M. & Svore, K. M. Factoring with qutrits: Shor's algorithm on ternary and metaplectic quantum architectures. *Phys. Rev. A* **96**, 012306 (2017).
6. Gokhale, P. et al. Asymptotic improvements to quantum circuits via qutrits. In *Proc. 46th International Symposium on Computer Architecture* https://doi.org/10.1145/3307650.3322253 (ACM, 2019).
7. Chu, J. et al. Scalable algorithm simplification using quantum AND logic. *Nat. Phys.* **19**, 126–131 (2023).
8. Fernández De Fuentes, I. et al. Navigating the 16-dimensional Hilbert space of a high-spin donor qudit with electric and magnetic fields. *Nat. Commun.* **15**, 1380 (2024).
9. Vilas, N. B. et al. An optical tweezer array of ultracold polyatomic molecules. *Nature* **628**, 282–286 (2024).
10. Chaudhury, S. et al. Quantum control of the hyperfine spin of a Cs atom ensemble. *Phys. Rev. Lett.* **99**, 163002 (2007).
11. Kues, M. et al. On-chip generation of high-dimensional entangled quantum states and their coherent control. *Nature* **546**, 622–626 (2017).
12. Chi, Y. et al. A programmable qudit-based quantum processor. *Nat. Commun.* **13**, 1166 (2022).
13. Nguyen, L. B. et al. Empowering a qudit-based quantum processor by traversing the dual bosonic ladder. *Nat. Commun.* **15**, 7117 (2024).
14. Roy, S. et al. Synthetic high angular momentum spin dynamics in a microwave oscillator. *Phys. Rev. X* **15**, 021009 (2025).
15. Wang, Z., Parker, R. W., Champion, E. & Blok, M. S. High-E_J/E_C transmon qudits with up to 12 levels. *Phys. Rev. Appl.* **23**, 034046 (2025).
16. Leupold, F. M. et al. Sustained state-independent quantum contextual correlations from a single ion. *Phys. Rev. Lett.* **120**, 180401 (2018).
17. Ringbauer, M. et al. A universal qudit quantum processor with trapped ions. *Nat. Phys.* **18**, 1053–1057 (2022).
18. Adambukulam, C., Johnson, B., Morello, A. & Laucht, A. Hyperfine spectroscopy and fast, all-optical arbitrary state initialization and readout of a single, ten-level ^{73}Ge vacancy nuclear spin qudit in diamond. *Phys. Rev. Lett.* **132**, 060603 (2024).
19. Soltamov, V. A. et al. Excitation and coherent control of spin qudit modes in silicon carbide at room temperature. *Nat. Commun.* **10**, 1678 (2019).
20. Gottesman, D., Kitaev, A. & Preskill, J. Encoding a qubit in an oscillator. *Phys. Rev. A* **64**, 012310 (2001).
21. Sivak, V. et al. Model-free quantum control with reinforcement learning. *Phys. Rev. X* **12**, 011059 (2022).
22. Sivak, V. V. et al. Real-time quantum error correction beyond break-even. *Nature* **616**, 50–55 (2023).
23. Wang, Y., Hu, Z., Sanders, B. C. & Kais, S. Qudits and high-dimensional quantum computing. *Front. Phys.* **8**, 589504 (2020).
24. Campbell, E. T., Anwar, H. & Browne, D. E. Magic-state distillation in all prime dimensions using quantum Reed-Muller codes. *Phys. Rev. X* **2**, 041021 (2012).
25. Campbell, E. T. Enhanced fault-tolerant quantum computing in *d*-level systems. *Phys. Rev. Lett.* **113**, 230501 (2014).
26. Meth, M. et al. Simulating two-dimensional lattice gauge theories on a qudit quantum computer. *Nat. Phys.* **21**, 570–576 (2025).
27. Sawaya, N. P. D. et al. Resource-efficient digital quantum simulation of *d*-level systems for photonic, vibrational, and spin-s Hamiltonians. *npj Quantum Inf.* **6**, 49 (2020).
28. Ofek, N. et al. Extending the lifetime of a quantum bit with error correction in superconducting circuits. *Nature* **536**, 441–445 (2016).
29. Ni, Z. et al. Beating the break-even point with a discrete-variable-encoded logical qubit. *Nature* **616**, 56–60 (2023).
30. Google Quantum AI and Collaborators. Quantum error correction below the surface code threshold. *Nature* **638**, 920–926 (2025).
31. Flühmann, C. et al. Encoding a qubit in a trapped-ion mechanical oscillator. *Nature* **566**, 513–517 (2019).
32. De Neeve, B., Nguyen, T.-L., Behrle, T. & Home, J. P. Error correction of a logical grid state qubit by dissipative pumping. *Nat. Phys.* **18**, 296–300 (2022).
33. Campagne-Ibarcq, P. et al. Quantum error correction of a qubit encoded in grid states of an oscillator. *Nature* **584**, 368–372 (2020).
34. Lachance-Quirion, D. et al. Autonomous quantum error correction of Gottesman–Kitaev–Preskill states. *Phys. Rev. Lett.* **132**, 150607 (2024).
35. Konno, S. et al. Logical states for fault-tolerant quantum computation with propagating light. *Science* **383**, 289–293 (2024).
36. Matsos, V. G. et al. Universal quantum gate set for Gottesman–Kitaev–Preskill logical qubits. Preprint at https://arxiv.org/abs/2409.05455 (2024).
37. Gertler, J. M. et al. Protecting a bosonic qubit with autonomous quantum error correction. *Nature* **590**, 243–248 (2021).
38. Place, A. P. M. et al. New material platform for superconducting transmon qubits with coherence times exceeding 0.3 milliseconds. *Nat. Commun.* **12**, 1779 (2021).
39. Ganjam, S. et al. Surpassing millisecond coherence in on chip superconducting quantum memories by optimizing materials and circuit design. *Nat. Commun.* **15**, 3687 (2024).
40. Reagor, M. et al. Quantum memory with millisecond coherence in circuit QED. *Phys. Rev. B* **94**, 014506 (2016).
41. Weyl, H. *The Theory of Groups and Quantum Mechanics* (Dover Publications, 1950).
42. Schwinger, J. Unitary operator bases. *Proc. Natl Acad. Sci. USA* **46**, 570 (1960).
43. Royer, B., Singh, S. & Girvin, S. Stabilization of finite-energy Gottesman-Kitaev-Preskill states. *Phys. Rev. Lett.* **125**, 260509 (2020).
44. Grimsmo, A. L. & Puri, S. Quantum error correction with the Gottesman-Kitaev-Preskill code. *PRX Quantum* **2**, 020101 (2021).
45. Flühmann, C. & Home, J. Direct characteristic-function tomography of quantum states of the trapped-ion motional oscillator. *Phys. Rev. Lett.* **125**, 043602 (2020).
46. Kenfack, A. & Życzkowski, K. Negativity of the Wigner function as an indicator of non-classicality. *J. Opt. B* **6**, 396 (2004).
47. Nielsen, M. A. A simple formula for the average gate fidelity of a quantum dynamical operation. *Phys. Lett. A* **303**, 249–252 (2002).
48. Eickbusch, A. et al. Fast universal control of an oscillator with weak dispersive coupling to a qubit. *Nat. Phys.* **18**, 1464–1469 (2022).
49. Rosenblum, S. et al. Fault-tolerant detection of a quantum error. *Science* **361**, 266–270 (2018).
50. Ding, A. Z. et al. Quantum control of an oscillator with a Kerr-cat qubit. Preprint at https://arxiv.org/abs/2407.10940 (2024).

51. Schmidt, F., Miller, D. & Van Loock, P. Error-corrected quantum repeaters with Gottesman–Kitaev–Preskill qudits. *Phys. Rev. A* **109**, 042427 (2024).
52. Wang, Z. & Jiang, L. Passive environment-assisted quantum communication with GKP states. *Phys. Rev. X* **15**, 021003 (2025).
53. Terhal, B. M., Conrad, J. & Vuillot, C. Towards scalable bosonic quantum error correction. *Quantum Sci. Technol.* **5**, 043001 (2020).
54. Schmidt, F. & van Loock, P. Quantum error correction with higher Gottesman–Kitaev–Preskill codes: minimal measurements and linear optics. *Phys. Rev. A* **105**, 042427 (2022).
55. Rojkov, I. et al. Two-qubit operations for finite-energy Gottesman–Kitaev–Preskill encodings. *Phys. Rev. Lett.* **133**, 100601 (2024).
56. Cafaro, C., Maiolini, F. & Mancini, S. Quantum stabilizer codes embedding qubits into qudits. *Phys. Rev. A* **86**, 022308 (2012).
57. Gross, J. A. Designing codes around interactions: the case of a spin. *Phys. Rev. Lett.* **127**, 010504 (2021).
58. Gross, J. A., Godfrin, C., Blais, A. & Dupont-Ferrier, E. Hardware-efficient error-correcting codes for large nuclear spins. *Phys. Rev. Appl.* **22**, 014006 (2024).

Methods

Phase update between stabilization rounds

The generalized SBS circuit in Fig. 1c realizes autonomous QEC of the finite-energy GKP code with respect to the ideal stabilizer $S_X = D(\sqrt{\pi d})$ (ref. 43). The analogous circuit for $S_Z = D(i\sqrt{\pi d})$ is obtained by updating the phase of all subsequent cavity operations by π/2, which transforms $q \to p$ and $p \to -q$ in the rotating frame of the cavity, where $q = (a + a^\dagger)/\sqrt{2}$ is the position of the cavity and $p = i(a^\dagger - a)/\sqrt{2}$ is the momentum. To mitigate the effects of experimental imperfections, we symmetrized the protocol by also performing QEC with respect to stabilizers $S_X^\dagger$ and $S_Z^\dagger$, which are related to the circuit in Fig. 1c by phase updates of π and 3π/2, respectively. The full protocol is periodic with respect to four SBS rounds, as each stabilizer ($S_X, S_Z, S_X^\dagger, S_Z^\dagger$) is measured once per period.

Ideally, we would measure the stabilizer S_X by implementing the ancilla-controlled-stabilizer operation CX_d^d, but in practice, we instead used $\mathrm{ECD}(\sqrt{\pi d}) = D(-\sqrt{\pi d}/2)CX_d^d\sigma_x$ (refs. 33,48). For even dimensions d, the extra displacement $D(-\sqrt{\pi d}/2)$ is the ideal Pauli operator $X_d^{d/2}$, the effect of which can be tracked in software (a similar result holds for the other stabilizers). In this case, we are free to measure the stabilizers in any order. We chose to increment the cavity phase in each round according to

$$\phi_j^{(d\ \mathrm{even})} = \pi/2, \tag{7}$$

which measures the stabilizers in the order S_X, S_Z, $S_X^\dagger$ and $S_Z^\dagger$. However, for odd d, the displacement $D(-\sqrt{\pi d}/2)$ takes us outside the code space, an effect we have to reverse before moving on to measure S_Z. To do so, we incremented the cavity phase in each round according to

$$\phi_j^{(d\ \mathrm{odd})} = \begin{cases} \pi, & j \equiv 0 \pmod 4, \\ -\pi/2, & j \equiv 1 \pmod 4, \\ \pi, & j \equiv 2 \pmod 4, \\ \pi/2, & j \equiv 3 \pmod 4, \end{cases} \tag{8}$$

which measures the stabilizers in the order S_X, $S_X^\dagger$, S_Z and $S_Z^\dagger$.

Compiling generalized controlled Pauli gates

The ancilla-controlled version of generalized Pauli operator $P_d = e^{i\varphi}X_d^n Z_d^m$ on the ideal GKP code is given by $CP_d = |g\rangle\langle g| + |e\rangle\langle e|\, e^{i\varphi}D(\beta_n)D(\beta_m)$, where $\beta_n = n\sqrt{\pi/d}$ and $\beta_m = im\sqrt{\pi/d}$. We compiled CP_d in terms of ancilla rotations and a single ECD gate:

$$\mathrm{ECD}(\beta_{nm}) = D(-\beta_{nm}/2)(|g\rangle\langle e| + |e\rangle\langle g|D(\beta_{nm})), \tag{9}$$

where $\beta_{nm} = \beta_n + \beta_m$. Using $D(\beta_{nm}) = \exp(inm\pi/d)D(\beta_n)D(\beta_m)$, this can be rewritten as

$$\mathrm{ECD}(\beta_{nm}) = D(-\beta_{nm}/2)\sigma_z(\varphi_{nm})CP_d\sigma_x, \tag{10}$$

where $\varphi_{nm} = nm\pi/d - \varphi$ and $\sigma_z(\theta) = |g\rangle\langle g| + |e\rangle\langle e|\, e^{i\theta}$. Rearranging terms, we obtain

$$CP_d = D(\beta_{nm}/2)\sigma_z(-\varphi_{nm})\mathrm{ECD}(\beta_{nm})\sigma_x. \tag{11}$$

In our experiments, we omitted the unconditional displacement $D(\beta_{nm}/2)$ when compiling CP_d gates, which affected the backaction of our GKP qudit logical measurements (Figs. 2 and 3). In addition, we used the smallest amplitude $|\beta_{nm}|$ consistent with the Pauli operator P_d. As an example, for $n = d-1$ and $d > 2$, we used $\beta_{nm} = -\sqrt{\pi/d} + im\sqrt{\pi/d}$ because $X_d^{d-1} = X_d^{-1}$. We emphasize that this CP_d gate is designed for the ideal GKP code and will necessarily incur infidelity when applied to the finite-energy code, but it may be possible to adapt this construction to the finite-energy case[32,43,55].

Optimizing the QEC protocol

To optimize our generalized SBS protocol (Fig. 1c), we followed the method described in ref. 22, parametrizing the SBS circuit using 45 free parameters in total. Anticipating that the larger conditional displacements required for GKP qudit stabilization (nominally proportional to $\sqrt{\pi d}$) would take longer to execute, we fixed the duration of each SBS round to be 7 μs (instead of 5 μs as in ref. 22).

We used a reinforcement learning agent to optimize our QEC protocol over these 45 parameters in a model-free way[21]. In each training epoch, the agent sends a batch of ten parametrizations $\mathbf{p}_i$ to the experiment, collects a reward R_i for each, and updates its policy to increase the reward. For our reward, we measured the probability that the QEC protocol keeps our logical qudit in its initial state, operationally quantified by

$$R_i = \frac{1}{2}\Big[\langle Z_0|\mathcal{E}_{\mathbf{p}_i}^N(|Z_0\rangle\langle Z_0|)|Z_0\rangle_d + \langle X_1|\mathcal{E}_{\mathbf{p}_i}^N(|X_1\rangle\langle X_1|)|X_1\rangle_d\Big], \tag{12}$$

where $\mathcal{E}_{\mathbf{p}_i}^N$ is the channel corresponding to N rounds of the SBS protocol parametrized by $\mathbf{p}_i$. For our optimal GKP qubit, we used $N = 140$ and 200 training epochs, for the qutrit, $N = 80$ and 200 training epochs, and for the ququart, $N = 80$ and 300 training epochs.

Regarding the scalability of this optimization method, we emphasize that the resources required for training our GKP qudits are the same as for the GKP qubit and that this training was implemented using off-the-shelf consumer electronics. Because the training was performed for individual qubits or qudits, we expect that it could be parallelized across an array of such systems, yielding a resource requirement that scales only linearly with the system size. We expect that applying reinforcement learning to optimize entangling gates will be more complicated than applying it to individual qubits or qudits.

Data availability

The data that support the findings of this study are available at Zenodo (https://doi.org/10.5281/zenodo.15009817)[59].

Code availability

The code used for reinforcement learning is available at GitHub (https://github.com/bbrock89/quantum_control_rl_server).

59. Brock, B. et al. Data for 'Quantum error correction of qudits beyond break-even'. *Zenodo* https://doi.org/10.5281/zenodo.15009817 (2025).

Acknowledgements We thank R. G. Cortiñas, J. Curtis, W. Dai, S. Hazra, A. Koottandavida, A. Miano, S. Puri, K. C. Smith and T. Tsunoda for helpful discussions. This research was sponsored by the Army Research Office (ARO; grant no. W911NF-23-1-0051), by the US Department of Energy (DoE), Office of Science, National Quantum Information Science Research Centers, Co-design Center for Quantum Advantage (contract no. DE-SC0012704) and by the Air Force Office of Scientific Research (AFOSR; award no. FA9550-19-1-0399). The views and conclusions contained in this document are those of the authors and should not be interpreted as representing the official policies, either expressed or implied, of the ARO, DoE, AFOSR or the US Government. The US Government is authorized to reproduce and distribute reprints for Government purposes notwithstanding any copyright notation herein. The use of fabrication facilities was supported by the Yale Institute for Nanoscience and Quantum Engineering and the Yale SEAS Cleanroom.

Author contributions B.L.B. conceived the experiment, performed the measurements and analysed the results. B.L.B. and S.S. developed the theory, with supervision from S.M.G. B.L.B. devised the generalized Pauli measurement protocols, with input from A.E. and S.S. V.V.S. provided the experimental set-up and wrote the reinforcement learning code.

A.E., V.V.S., A.Z.D. and L.F. provided experimental support throughout the project. M.H.D. supervised the project. B.L.B. and M.H.D. wrote the manuscript, with feedback from all authors.

Competing interests L.F. is a founder and shareholder of Quantum Circuits, Inc. S.M.G. is an equity holder in and receives consulting fees from Quantum Circuits, Inc. M.H.D. has an advisory role at Google Quantum AI. The other authors declare no competing interests.

Additional information

Supplementary information The online version contains supplementary material available at https://doi.org/10.1038/s41586-025-08899-y.

Correspondence and requests for materials should be addressed to Benjamin L. Brock or Michel H. Devoret.

Peer review information *Nature* thanks the anonymous reviewers for their contribution to the peer review of this work.